Journal of Geophysics and Engineering, 2025, **22**(2), 631–639
https://doi.org/10.1093/jge/gxaf030
Advance access publication date: 2025 March 11
Research Article

OXFORD

Evidence of shallow large earthquake associated with fault linkage

Liang Chen[1], Xingguo Huang[2,*], Cong Wang[2], Xiao-Bi Xie[3], Hancheng Ji[1], Stewart Greenhalgh[4], Jinping Zi[5], and Hongfeng Yang[5]

[1]State Key Laboratory of Petroleum Resources and Prospecting, China University of Petroleum, Beijing 102249, China
[2]Jilin University, College of Instrumentation and Electrical Engineering, Changchun 130061, China
[3]University of California, Earth and Planetary Sciences, Modeling and Imaging Laboratory, 1156 High Street, Santa Cruz, CA 95064, USA
[4]Swiss Federal Institute of Technology (ETH) Zurich, Institute of Geophysics, Department of Earth Sciences, Zurich 8092, Switzerland
[5]Department of Earth and Environmental Sciences, Chinese University of Hong Kong, Sha Tin, Hong Kong 999077, China

*Corresponding author. Jilin University, College of Instrumentation and Electrical Engineering, Changchun, China, E-mail: xingguohuang@jlu.edu.cn

Abstract

Tectonic earthquakes are usually thought to be the result of stick-slip frictional instability along a pre-existing fault. As a result, large earthquakes rarely nucleate at shallow depths. In the present study, we relocated the 8 September 2019 Ms 5.4 earthquake in Weiyuan, Sichuan, China, and 943 aftershocks. The results suggest rather surprisingly that these seismic events occurred at a depth of less than 3.5 km, rupturing the relay zone between two active thrust faults. Prior to the Ms 5.4 earthquake, the ruptured relay ramp zone was subjected to abnormally high shear stress, as demonstrated by our stress field modeling. This indicates that the two active faults are strongly interacted and prone to connect. The increased shear stress caused strong elastic accumulation and thus induced the Ms 5.4 earthquake. We believe this mechanism should garner widespread attention, particularly for shallow earthquake assessment.

Keywords: hydraulic fracturing; fault interpretation; elastic accumulation; stress field; large earthquake

1. Introduction

Large earthquakes are commonly thought to nucleate in the deep portion of the seismogenic layer (Das & Scholz 1983). This is due to the fact that tectonic earthquakes primarily result from the stick-slip frictional instability along a pre-existing fault surface, rather than the creation of a new fault and fracture (Scholz 1998). In friction stability regimes, elastic strain gradually accumulates over the inter-seismic interval until it exceeds the frictional rock strength, which increases with depth together with the normal stress and stress drop (Brace & Byerlee 1966). Indeed, moderate-to-large earthquakes do occur at extremely shallow depths (Yang & Yao 2021), such as the 1968 Ms 6.8 Meckering earthquake in Western Australia (Langston 1987), the 2008 Ms 5.7 aftershock of the Mw 7.9 Wenchuan earthquake (Luo *et al*. 2010), the 2019 Mw 4.9 Le Teil earthquake in France (Causse *et al*. 2021), and the 2020 Mw 6.5 Monte Cristo Range earthquake in Nevada (Sethanant *et al*. 2023). The above events are interpreted with distinctively particular seismogenesis, which lacks general significance for shallow earthquake assessment. Conversely, there are difficulties in the interpretation of extremely shallow earthquakes and investigation of seismogenic structures, because of the complex subsurface structure and the often poorly constrained velocity models (Huang *et al*. 2022).

The 8 September Weiyuan 2019 Ms 5.4 earthquake in Sichuan, China caused 64 casualties and destroyed 293 buildings, resulting in 680 sq km of devastation. The hypocenter and centroid of this earthquake source zone were located at between 2.4 and 4.5 km beneath the surface, as reported by previous investigations (Lei *et al*. 2020; Sheng *et al*. 2020; Wang *et al*. 2020; Yi *et al*. 2020; Zi *et al*. 2025). Another extremely shallow 2019 Ms 6.0 earthquake in Changning, South Sichuan Basin, China, has been studied and is thought to be triggered by the combined effect of pore pressure increase from the diffusion of injected fluids. Although it has been suggested that the Weiyuan 2019 Ms 5.4 earthquake was also induced by hydraulic fracturing during the shale gas development in the Weiyuan gas field, there is still a lack of solid evidence, and the seismogenic fault remains unknown. In the Weiyuan area, we have a depth-domain 3D exploration seismic reflection data set acquired in 2015, coupled with well logs. Using the 3D seismic data and the accompanying sonic well logs, a high precision interval-velocity-constrained velocity model was obtained. We have re-located the Weiyuan Ms 5.4 earthquake and 943 correlated aftershocks using the interval-velocity-constrained velocity model and identified the seismogenic structure from the 3D seismic reflection images.

2. Geological settings

The 8 September 2019 Ms 5.4 earthquake occurred in the Weiyuan Anticline, Sichuan, China, which is surrounded by the Longquan Mountain structural belt in the west (Fig. 1a), the central Sichuan monocline in the north, and the Zigong Sag in the south, was formed during the Himalayan era (Li *et al*. 2015). The lithology of the sedimentary strata has been revealed through hydrocarbon boreholes that penetrate the Cambrian formation. The emerged terrane is Jurassic sandstone and mudstone, which are underlain by Triassic,

Received: September 29, 2024. **Revised:** February 13, 2025. **Accepted:** March 10, 2025

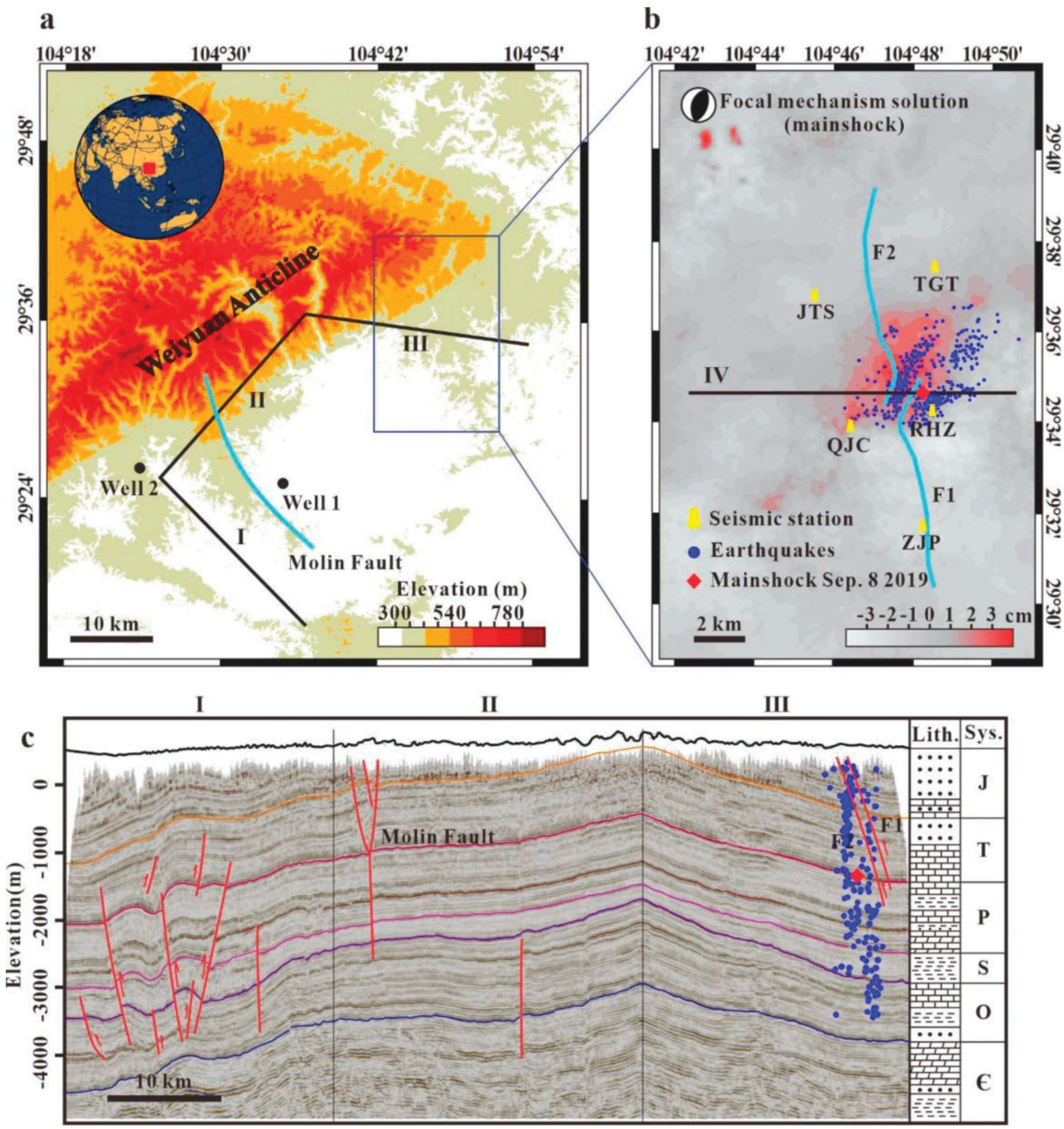

Figure 1. Location map and seismic profile. (a) Elevation map showing the location of Weiyuan Anticline, the regional seismic profile, exploration wells, and the key surface structure. (b) Coseismic deformation of the 8 September 2019 earthquake showing the location of the mainshock and aftershocks, the focal mechanism solution of the mainshock (Lei *et al.* 2020; Jia *et al.* 2023), and the fault trace of the seismogenic faults. (c) Regional seismic profile showing the subsurface structures, studied earthquakes, and the lithology of subsurface intervals. The emerged terrane is Jurassic sandstone and mudstone (J), which are underlain by Triassic (T), Permian (P), Silurian (S), Ordovician (O), and Cambrian sediments (C).

Permian, Silurian, Ordovician, and Cambrian sediments (Fig. 1c) (Liang *et al.* 2019). These underlying beds dip to the south and are truncated northwards at the Weiyuan Anticline. In the southwest of the dome structure, several folds were developed during Permian, Silurian, Ordovician, and Cambrian successions. The Weiyuan Anticline is located in the transition zone of the movement of the South China plate (Zhang 2013), and the stress tests in the horizontal wells, at a depth range of around 3 km, indicates that the southern area of the Weiyuan Anticline has a maximum horizontal stress of approximately 90 MPa oriented southwest (Xi *et al.* 2018). At the southern flank of the Weiyuan Anticline, several southeast trending faults have been geologically mapped by geological survey (Fig. 1a).

3. Methods

3.1. Processing information of the 3D seismic data

The depth-domain 3D reflection seismic data set was used in this work. This dataset covers an area of over 1925 sq km in the south of the Weiyuan Anticline, with an investigation depth of 5 km. The seismic data was resampled to 1 ms before processing, and the base level was set to 1000 m with a replacement velocity of 4000 m/s. Tomographic static correction was performed with maximum and minimum offsets of 3500 m and 300 m, respectively. Coherent noise reduction (0~16 Hz, 800~1800 m/s) was employed for the pre-stack data, and the post-stack seismic data was bandpass filtered (7–79 Hz). Kirchhoff pre-stack depth migrations were carried out based on the velocity model derived from root-mean-square

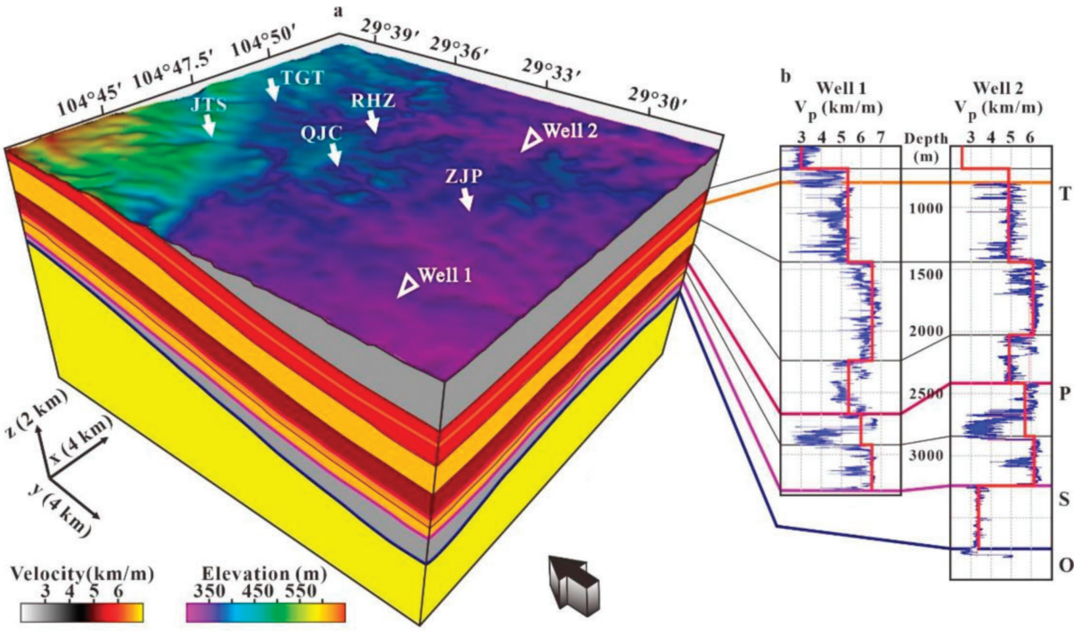

Figure 2. Interval-velocity-constrained velocity model. (a) Three-dimensional display of the velocity model showing the velocity framework and key reflection surfaces. (b) P-wave sonic log of drill wells. The well location is marked in Fig. 1a.

stacking velocities. The resulting depth image was used to interpret the various geological horizons and seismogenic structure.

3.2. Earthquake relocation

Because of the complicated subsurface structure developed in the Weiyuan area, using a simple 1D velocity model to locate such shallow earthquakes may not yield hypocenters to a sufficiently high resolution. For the Ms 5.4 earthquakes, Wang *et al.* (2020) used a single crustal velocity model to determine the focal depth at 5 km, close to the result (4.5 km) of Yi *et al.* (2020) employing a different 1D layered velocity model. Notably, two other studies provided different focal depths of 2.5 km (Lei *et al.* 2020) and 2.9 km (Sheng *et al.* 2020), respectively. Therefore, we decided to build a high-resolution interval-velocity-constrained velocity model with an area of 400 sq km covering the local seismic network and earthquakes under study, to improve the accuracy of earthquake location.

First, we interpret the horizons that separate the subsurface formations with different P-wave velocity to construct a stratigraphic framework (Fig. 2a). This framework defines the critical interfaces for determining the ray travel paths. The interval velocity is determined using sonic well logs provided by the Southwest Oil-Gas Field Company (Fig. 2b). An average velocity is calculated for each formation. Then, we create an interval-velocity-constrained velocity model for the mainshock that defines a 20-kilometer-long square. Within the interval-velocity-constrained velocity model, five seismic stations are situated.

The catalog provided by the Sichuan Seismological Bureau, China, suggests that few foreshocks were recorded prior to the mainshock on 8 September 2019. Therefore, we picked all the aftershocks occurring in September 2019, which are reported in the areal extent of the interval-velocity-constrained velocity model. The hypocenter location method we used is the Source-Scanning Algorithm proposed by Kao and Shan (Kao *et al.* 2005). Consequently, we located 943 events. Among the located events, 500 are in the extent of the velocity model including the mainshock and aftershocks in September 2019 (Fig. 1b), and the others are outside of the investigation and were not located.

3.3. Fault interpretation and activity

We image the subsurface structures surrounding the studied earthquake cluster on structure maps of key horizons, as well as the seismogenic faults. The horizon and fault interpretation are conducted through the 3D seismic data using the seismic interpretation module of Petrel 2018. Since the seismic data was acquired in 2015, the seismic images only capture the structural features present before the mainshock. Herein, the tops of the Triassic, Permian, Silurian, Ordovician, and Cambrian units are interpreted (Fig. 3). The prominent features we imaged on the structure maps indicate that the intervals south of the Weiyuan Anticline are a monocline dipping south with associated folds (Fig. 3). The seismogenic faults extend from the bottom of the Triassic to the Earth's surface. Two seismic reflectors, including the tops of the Triassic and Permian beds, are selected to generate the fault throw profile of the seismogenic structure. The fault throw profile is used to qualitatively estimate the fault activity.

3.4. Coseismic deformation

The coseismic deformation of the Ms 5.4 earthquake, shown in Fig. 1b, was investigated with the interferometric synthetic aperture radar (InSAR) technique. In the present study, the C band data of Sentinel-1A is used as the source of SAR data for the InSAR analysis. The sensor of the Sentinel-1 has a frequency of 5.4 GHz corresponding to a wavelength of 5.6 cm. Four Sentinel-1 Single Look Complex (SLC) products in IW mode with VV polarization were acquired from the

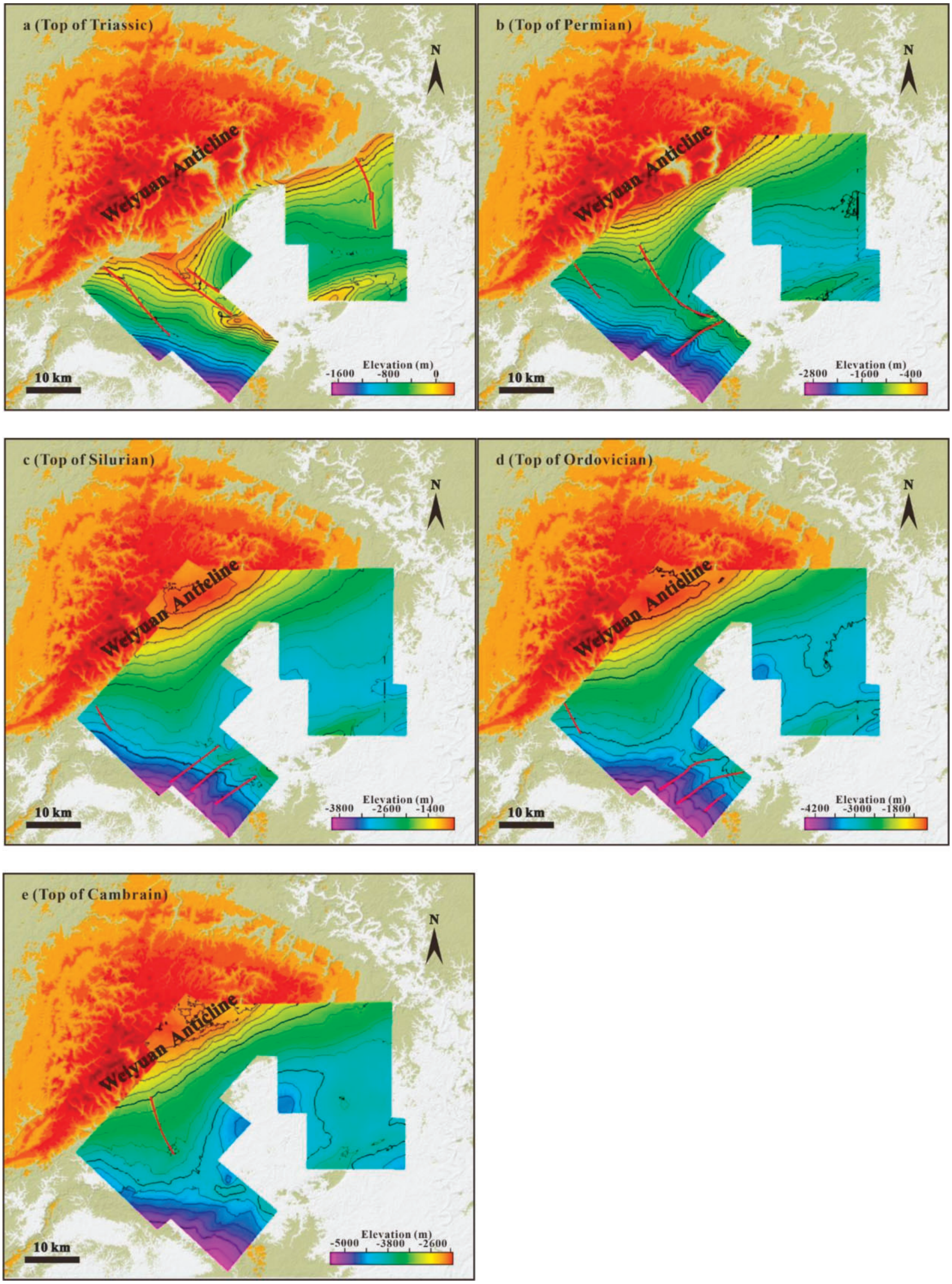

Figure 3. Structure maps of the key horizons and features present before the mainshock.

Alaska Satellite Facility, and the corresponding orbit files were obtained from the European Space Agency. The SLC products with date of September 1, 2019, and September 13, 2019, were utilized to analyze the surface deformation caused by the mainshock that occurred on September 8, 2019. The SRTM digital elevation model with a resolution of 30 m was employed to simulate the topographic phase. The InSAR analysis processing was conducted by the GAMMA 2015 Software in a Linux operating system (Ubuntu 16.04) to generate the interferograms. The after-earthquake SLC product was set as the main image for interferogram generation. The interferograms were filtered using the noise files attached with the SLC products. The filtered interferograms were used to detect the location of surface deformation and estimate the deformation extent. We then unwrapped the interferogram using the minimum cost network method and geocoded the unwrapped interferogram into the WGS84 coordinate system.

3.5. Stress field modeling

Our modeling study was conducted using Ploy3D (Thomas 1993) software integrated with the structure modeling module of Petrel 2018, which is a boundary element program based on linear elasticity theory. This method has been used to model fault displacement, strain and stress distribution around faults. The advantage of this method is that only the fault surface needs to be discretized rather than the entire volume.

The fault surface used in the modeling is imaged using the seismic interpretation module of Petrel 2018 from the 3D seismic data. Triaxial compressive remote stresses are used as the boundary condition for the modeling, and zero displacement boundary condition along the modeled fault is used. The remote stresses are determined using the adjacent horizontal hydrocarbon wells. The maximum horizontal principal stress (σ_{H}) perpendicular to the seismogenic faults is set to 90 MPa, whereas the minimum horizontal principal stress (σ_{h}) is set to 70 MPa. Additionally, the faults are subjected to a vertical stress (σ_{V}) caused by the load of sedimentary rocks, such as $\sigma_{\mathrm{V}} = \rho gz$, where ρ is the density of the sedimentary rocks, g is the gravitational acceleration and z is the depth. We use an average σ_{V} of 39 MPa in our modeling, with ρ and z of 2800 kg/m^3 and 1000 m, respectively. A Poisson's ratio ($\mu = 0.25$) defines the material properties of the fault blocks. These conditions produce a remote stress field in which $\sigma_1 = \sigma_{\mathrm{H}}, \sigma_2 = \sigma_{\mathrm{h},}$ and $\sigma_3 = \sigma_{\mathrm{V}}$. The along strike variation of the fault displacement, strain and stress distribution are calculated using Poly3D (Thomas 1993).

In order to assess the potential of shear stress failure, we calculated the maximum Coulomb shear stress (S_c) in the modeling rock volume. The maximum Coulomb shear stress is a criterion for shear failure in linear elasticity theory (Jaeger & Cook 1979), which is defined as

$$Sc = \frac{\sigma_1 - \sigma_3}{2} * \sqrt{1+n^2}) - n * \frac{\sigma_1 + \sigma_3}{2}, \tag{1}$$

where n is the coefficient of internal friction ($n = 0.6$).

4. Result

4.1. Seismological observation on the Ms 5.4 earthquake in Weiyuan, Sichuan, China

After relocation of the hypocenter using the interval-velocity-constrained velocity model constructed from 3D exploration seismic reflection data and sonic well logs, the mainshock and accompanying aftershocks sequence foci in September 2019 were determined, and the trend of the cluster is northeastern (Figs 1b and 4e). The relocated aftershock hypocenters are shallower than 3.5 km, whereas the hypocenter of the Ms 5.4 mainshock is 2.2 km deep (Fig. 3a); however, aftershocks appear to deviate from the interpreted fault planes. This may be due to location uncertainties during the earthquake relocation. The uncertainty was assessed by using the average deviation distance and the location bias caused by velocity field heterogeneity. If the deviation distance falls within the range of location error, the result is considered to be reasonable. By utilizing the functionalities in Petrel, the vertical distance from all seismic events to the fault plane can be determined. We define distances toward the west side of the fault plane as negative values and those toward the east side as positive values. The average value we calculated is −1.43 km. According to the location results, the average arrival time of the seismic events observed by the five stations is 0.4 seconds. A velocity change of 1 km/s can produce a location error of 400 m. Within the depth range of the study area, the difference between the maximum and minimum P-wave velocities is approximately 4 km/s. Therefore, if there is significant velocity heterogeneity within the layer, it can cause an error of 1.4 km in the positioning results. This suggests that the uncertainties error may be contributing to the current results. The aftershocks gradually ruptured away from the mainshock to the shallow and deep portions along the seismogenic faults (Fig. 4b). Meanwhile, the magnitudes of the aftershocks decrease with distance away from the mainshock (Fig. 4c), but the aftershocks above the depth of the mainshock have lower magnitudes than the aftershocks deeper than the mainshock (Fig. 4c).

The focal mechanism solution indicates that the hypocenter is 2.48 km deep and the seismogenic structure is a thrust fault with a strike of 191° and a dip of 39° (Lei *et al.* 2020). Consistently, the profile taken perpendicular to the trend of the earthquake cluster shows a fault with a low dip angle, tilting southeast (Fig. 4b and c). According to InSAR data, the coseismic deformation generated by the Ms 5.4 shock results in a southwest-striking elliptical zone with a maximum uplift of approximately 3.5 cm (Fig. 1b).

4.2. Seismogenic structure of the Ms 5.4 earthquake

We can image the seismogenic structure using the 3D seismic data and describe the fault activities based on the variations along strike fault throw. The seismogenic structure of the Ms 5.4 earthquake is composed of two thrust faults, F1 to the south and F2 to the north, which are segmented by a relay ramp measuring 3 km in length and 800 m in width (Fig. 1b). These two faults are imaged to a depth of 2.5 km (Fig. 4b and c) and a length of 10 km, and the strike direction of the fault trace on the surface changes from NS to NE along the relay ramp (Fig. 1b). The segmented relay ramp is where the correlated events and coseismic deformation are located (Figs 1b and 4a). The steeper gradient of displacement profile seen at the relay ramp indicates that the activity of faults F1 and F2 is interacting prior to the mainshock (Fig. 5) (Gawthorpe & Leeder 2000). The displacement variation of the tops of the Triassic and Permian sequences are quite parallel with each

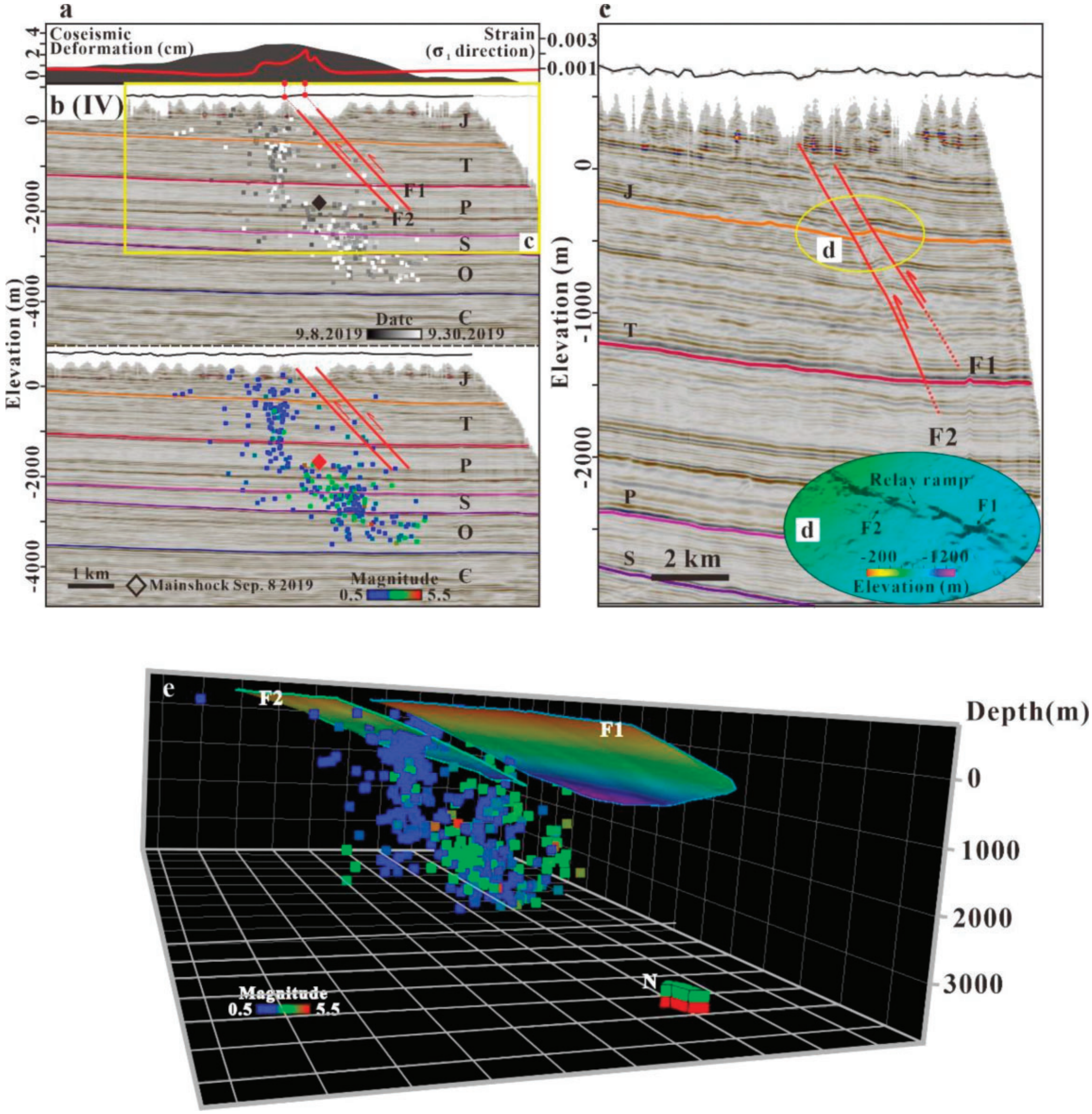

Figure 4. Seismicity and seismic reflection images. (a) Cross section of the coseismic deformation and modeled strain variation along the seismic profile. (b) Seismic profile projected with the seismicity and the seismogenic faults. The dates and magnitudes are marked by colors, and the profile location is shown in Fig. 1b. (c) Zoomed seismic profile showing the details of the seismogenic faults. (d) Three-dimensional display of the top of the Triassic sequence showing the relay ramp between F1 and F2.

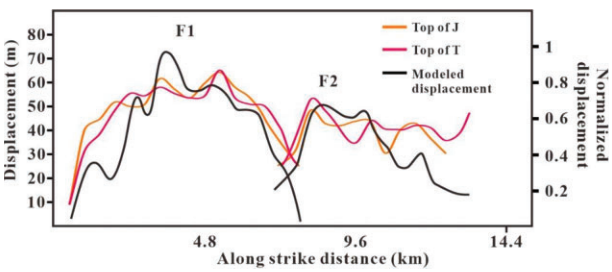

Figure 5. Displacement profile. The displacements of the tops of the Triassic and Permian units are measured along F1 and F2 from the 3D seismic reflection data. The modeled displacement is also projected onto the profile with the normalized value.

other in both trend and value. This suggests that the faults started to be active after the deposition of Jurassic units.

It is commonly thought that earthquakes induce stress changes on neighboring faults, which can alter the probability of occurrence of future earthquakes (Harris & Simpson 1992; Stein *et al.* 1992; Harris 1998). The other fact in terms of faults is that the shear stress will drop extremely adjacent to a single normal fault, except near the fault tips where the shear stress notably increases (Segall & Pollard 1980; Willemse *et al.* 1996). For two interacting faults, the stress field can be quite perturbed within the interaction zone (Crider & Pollard 1998; Gupta & Scholz 2000). The modeling results of the pre-event stress field surrounding the seismogenic faults show that the seismogenic faults, although they are reverse faults, perturb the local stress field, resulting in increased strain in the relay ramp and fault tips (Fig. 6a). The strain shadow appears in the hanging wall and footwall of the thrust faults. Away from the stress shadow zone, the stain increases to the initial state (Fig. 6a). Stress perturbation is manifest in the relay ramp along the fault surface in the cross section (Fig. 6a). In linear elasticity theory, the maximum Coulomb shear stress (S_c) is given as the failure condition for shear failure (Jaeger & Cook 1979; Crider & Pollard 1998; Soliva *et al.* 2006). Our stress

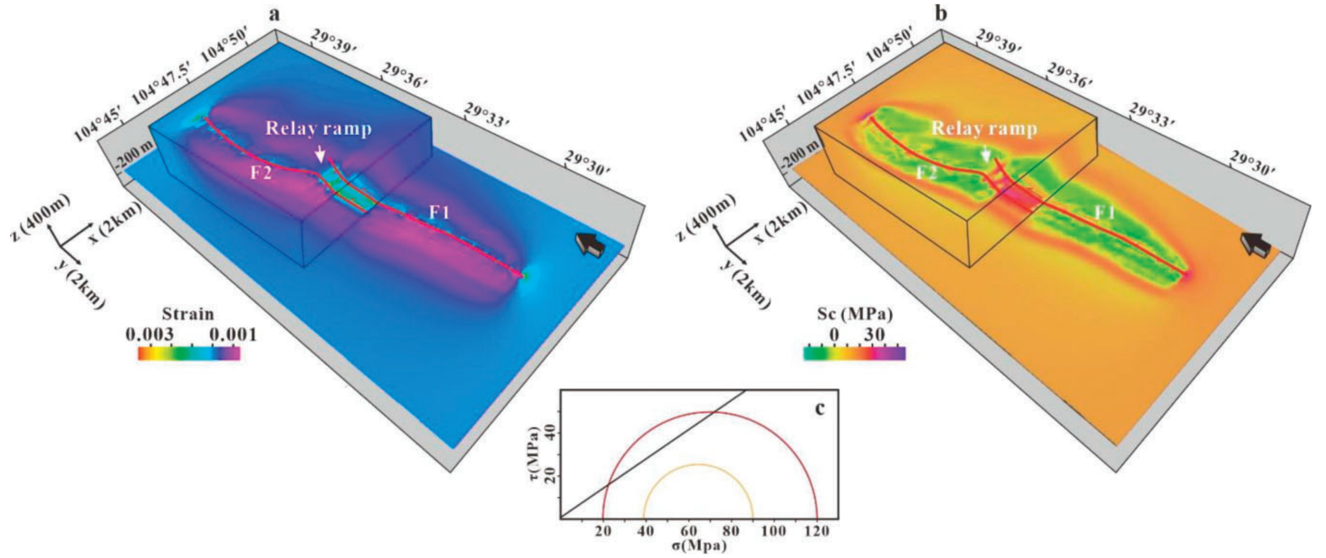

Figure 6. Stress modeling and Coulomb-Mohr diagram. Strain of σ_1 direction (a) and Sc (b) distributions of the stress modeling showing the strain and Sc perturbation in sections across the relay ramp and a horizontal slice at −200 elevation. (c) Coulomb-Mohr diagram showing the Mohr's circles specifically for the relay zone at an elevation of -200 m and the remote stress field with the red and yellow semi-circles, respectively, and the black line representing the Coulomb-Mohr failure envelope of tight sandstone, which is the representative lithology of the seismogenic layers.

modeling demonstrates a significant rise in S_c in the relay ramp zone (Fig. 6b). The Coulomb-Mohr diagram also shows the remote stress field fails to satisfy the Coulomb-Mohr failure criterion, whereas the relay zone does (Fig. 6c). It implies that the relay ramp has a high possibility for shear failure prior to the mainshock.

5. Discussion

Hydraulic fracturing (HF) usually induces earthquakes with small moment magnitude. Recently, induced earthquakes with $M_w > 4$ by HF have been reported (Babaie *et al.* 2019; Eyre *et al.* 2019; Lei *et al.* 2020; Wang, Harrington *et al.* 2020; Zhang *et al.* 2022; Igonin *et al.* 2023; Bhadran *et al.* 2024; Ng *et al.* 2024). Previous research hypothesized that the Ms 5.4 earthquake was caused by HF, as the seismogenic time and location coincided with the HF operation (Lei *et al.* 2020; Wang *et al.* 2020). We argue that because the HF-induced earthquakes are commonly thought to nucleate on faults beneath the HF formation (Bao & Eaton 2016; Lei *et al.* 2017; Skoumal *et al.* 2018), whereas the Ms 5.4 earthquake nucleates above the HF Silurian Longmaxi Formation (Fig. 1c). Sometimes the HF-induced earthquake could be triggered by aseismic slip caused above the fractured formation, such as the long-lived swarm in Fox Creek, Alberta, Cannada (Eyre *et al.* 2019). This long-lived seismic swarm is explained as the aseismic slip within the underlying HF-fractured stable formation, which leads to the upper distal unstable region of the fault being loaded. For the present event in Weiyuan, the HF operation is focused on the Longmaxi Formation, Silurian System, which is also a stable shale unit. However, observation shows that the seismogenic faults do not penetrate the Longmaxi Formation, and the lower distal region of the seismogenic faults has a vertical distance of 1500 km from the Longmaxi Formation. Therefore, it is difficult to explain the Weiyuan earthquake using the aseismic slip model. The fluid injection also hardly affects the upper seismogenic faults. Because there are two low permeability layers, the Upper Permian shale and the Silurian shale, respectively, without the linkup by faults, vertical fluid migration to the seismogenic layers is unlikely.

It is widely believed that large earthquakes do not nucleate at shallow depth due to the low normal stress and the resulting weak frictional strength of the rocks as well as the low stress drop (Das & Scholz 1983). This results in insufficient elastic strain energy accumulation at shallow depth to trigger large earthquakes. Faults are not always independent and isolated structures, and the segmented faults could have strong interaction before their full linkage (Crider & Pollard 1998; Cowie *et al.* 2000; Gawthorpe & Leeder 2000; Liu *et al.* 2017; Zaccaginio & Doglionni 2023). In relay ramps, fault interaction causes a steep displacement gradient (Peacock & Sanderson 1991; Gawthorpe & Leeder 2000), an increased local shear stress (Crider & Pollard 1998), and a rapid slip rate (Cowie & Roberts 2001). Before the relay ramp rupture and attendant fault linkage, the relay ramp zone must accumulate higher elastic strain than other regions along the fault. The increased local shear stress in unruptured relay ramps between interacting faults is therefore an important mechanism for the accumulation of elastic energy (Crider & Pollard 1998; Soliva *et al.* 2008). This increase in local shear stress is unrelated to the normal stress and hence the depth; it is governed solely by the relationship between displacement and spacing in the relay ramp (Soliva & Benedicto 2004). Structural geologists believe that the strong interacting relay ramp is vulnerable to seismic activity (Soliva & Benedicto 2004; Soliva *et al.* 2008). Our results indicate that instead of fault surface friction, for the shallow Ms 5.4 earthquake, the high elastic strain accumulation and shear stress are the result of the fault interaction.

6. Conclusions

The seismogenic structure is a relay ramp between two thrust faults penetrating to a depth of 2.5 km. Through stress field modeling, we reveal that the relay ramp ruptured by the mainshock was subjected to abnormally high shear stress approaching the shear brittle fracture criterion before the 8 September 2019 Ms 5.4 earthquake. This mechanism enables relay ramp structures to become seismically active zones for moderate to large earthquakes at extremely shallow depths. Due to the shallow focal depth and strong generation of surface waves, such earthquakes will cause more devastation, and similar structures should therefore be given special consideration during seismic hazard assessment. Our finding provides a seismogenesis for shallow earthquakes and offers a new perspective on seismic hazard assessment.

Funding

This work is supported by the Innovation Fund of China National Petroleum Corporation (grant no. 2021D002-0102), the Science Foundation of China University of Petroleum, Beijing (grant no. 2462023BJR011), National Natural Science Foundation of China (grant no. 42374149), Deep Earth National Science and Technology Major Project (grant no. 2024ZD1002807), National Natural Science Foundation of China (grant no. U2139203), and the Research Grants Council, University Grants Committee, Hong Kong (grant nos. 14303721, 14306122). The Sichuan Seismological Bureau, China, is gratefully acknowledged for the support of the earthquake catalog.

Conflict of interest statement

None declared.

Data availability

The data will be shared on reasonable request to the authors.

References

Babaie Mahani A, Kao H, Atkinson GM, Assatourians K, Addo K, Liu Y. 2019. Ground-motion characteristics of the 30 November 2018 injection-induced earthquake sequence in northeast British Columbia, Canada. *Seismol Res Lett*, **90**:1457–67. https://doi.org/10.1785/0220190040

Bao X, Eaton DW. 2016. Fault activation by hydraulic fracturing in Western Canada. *Science*, **354**:1406–9. https://doi.org/10.1126/science.153.3739.990

Bhadran A, Duarah BP, Girishbai D, Achu AL, Lahon S, Jesiya NP, Vijesh VK *et al.* 2024. Multi-model seismic susceptibility assessment of the 1950 great Assam earthquake in the Eastern Himalayan front. *Geosystems Geoenvironment*, **3**:100270. https://doi.org/10.1016/j.geogeo.2024.100270

Brace WF, Byerlee JD. 1966. Stick-slip as a mechanism for earthquakes. *Science*, **153**:990–2. https://doi.org/10.1126/science.aag2583

Causse M, Cornou C, Maufroy E, Grasso J, Baillet L, El Haber E. 2021. Exceptional ground motion during the shallow Mw 4.9 2019 Le Teil earthquake, France. *Commun Earth Environ*, **2**:1–9. https://doi.org/10.31226/osf.io/yq4dt

Cocco M, Nostro C, Ekström G. 2000. Static stress changes and fault interaction during the 1997 Umbria-Marche earthquake sequence. *J Seismolog*, **4**:501–16. https://doi.org/10.1023/A:1026507917308

Cowie PA, Gupta S, Dawers NH. 2000. Implications of fault array evolution for synrift depocentre development: insights from a numerical fault growth model. *Basin Res*, **12**:241–61. https://doi.org/10.1111/j.1365-2117.2000.00126.x

Cowie PA, Roberts GP. 2001. Constraining slip rates and spacings for active normal faults. *J Struct Geol*, **23**:1901–15. https://doi.org/10.1016/S0191-8141(01)00036-0

Crider JG, Pollard DD. 1998. Fault linkage: three-dimensional mechanical interaction between echelon normal faults. *J Geophys Res*, **103**:24373–91. https://doi.org/10.1029/98JB01353

Das S, Scholz CH. 1983. Why large earthquakes do not nucleate at shallow depths. *Nature*, **305**:621–3. https://doi.org/10.1038/305621a0

Eyre TS, Eaton DW, Garagash DI, Zecevic M, Venieri M, Weir R, Lawton DC, 2019. The role of aseismic slip in hydraulic fracturing–induced seismicity. *Sci Adv*, *5*: eaav7172. https://doi.org/10.1126/sciadv.aav7172

Gawthorpe RL, Leeder MR. 2000. Tectono-sedimentary evolution of active extensional basins. *Basin Res*, **12**:195–218. https://doi.org/10.1111/j.1365-2117.2000.00121.x

Gupta A, Scholz CH. 2000. A model of normal fault interaction based on observations and theory. *J Struct Geol*, **22**:865–79. https://doi.org/10.1016/S0191-8141(00)00011-0

Harris RA. 1998. Introduction to special section: stress triggers, stress shadows, and implications for seismic hazard. *J Geophys Res Solid Earth*, **103**:24347–58. https://doi.org/10.1029/98JB01576

Harris RA, Simpson RW. 1992. Changes in static stress on southern California faults after the 1992 Landers earthquake. *Nature*, **360**:251–4. https://doi.org/10.1038/360251a0

Huang XG, Greenhalgh S, Li H, Liu X. 2022. Generalized effective biot theory and seismic wave propagation in anisotropic, poroviscoelastic media. *J Geophys Res Solid Earth*, **127**:e2021JB023590. https://doi.org/10.1029/2021JB023590

Igonin N, Trugman DT, Gonzalez K, Eaton DW. 2023. Spectral characteristics of hydraulic fracturing-induced seismicity can distinguish between activation of faults and fractures. *Seismol Res Lett*, **94**:1791–806. https://doi.org/10.1785/0220230024

Jaeger JC, Cook NGW. 1979. *Fundamentals of Rock Mechanics*, 3rd edn. London: Chapman and Hall. https://doi.org/10.1016/0013-7952(77)90007-2

Jia XC, Li SL, Liu ZM, Gong C. 2023. Normative expression and accurate understanding of focal mechanism parameters. *Geosystems Geoenvironment*, **2**:100154. https://doi.org/10.1016/j.geogeo.2022.100154

Kao H, Shan S, Dragert H, Rogers G, Cassidy JF, Ramachandran K. 2005. A wide depth distribution of seismic tremors along the northern Cascadia margin. *Nature*, **436**:841–4. https://doi.org/10.1038/nature03903

Langston CA. 1987. Depth of faulting during the 1968 Meckering, Australia, earthquake sequence determined from waveform analysis of local seismograms. *J Geophys Res Solid Earth*, **92**:11561–74. https://doi.org/10.1029/JB092iB11p11561

Lei X, Huang D, Su J, Jiang G, Wang X, Wang H, Guo X *et al.* 2017. Fault reactivation and earthquakes with magnitudes of up to Mw 4.7 induced by shale-gas hydraulic fracturing in Sichuan Basin, China. *Sci Rep*, **7**:7971–12. https://doi.org/10.1029/JB092iB11p11561

Lei X, Su J, Wang Z. 2020. Growing seismicity in the Sichuan Basin and its association with industrial activities. *Sci China Earth Sci*, **63**:1633–60. https://doi.org/10.1007/s11430-020-9646-x

Li Z, Liu J, Li Y, Hang W, Hong H, Ying D, Chen X *et al.* 2015. Formation and evolution of Weiyuan-Anyue tensional corrosion trough in Sinian system, Sichuan Basin. *Pet Explor Dev*, **42**:29–36. https://doi.org/10.1016/S1876-3804(15)60003-9

Liang X, Liu S, Wang S, Deng B, Zhou S, Ma W. 2019. Analysis of the oldest carbonate gas reservoir in China—new geological significance of the Dengying gas reservoir in the Weiyuan Structure, Sichuan Basin. *J Earth Sci*, **30**:348–66. https://doi.org/10.1007/s12583-017-0962-y

Liu Y, Chen Q, Wang X, Hu K, Cao S, Wu L, Gao F. 2017. Influence of normal fault growth and linkage on the evolution of a rift basin; a case from the Gaoyou Depression of the Subei Basin, eastern China. *AAPG Bull*, **101**:265–88. https://doi.org/10.1306/06281615008

Luo Y, Ni S, Zeng X, Zheng Y, Chen Q, Chen Y. 2010. A shallow aftershock sequence in the north-eastern end of the Wenchuan

earthquake aftershock zone. *Sci China Earth Sci*, **53**:1655–64. https://doi.org/10.1007/s11430-010-4026-8
Ng R, Chen X, Nakata N, Walter JI. 2024. Precise relative magnitude measurement improves fracture characterization during hydraulic fracturing. *Geophys J Int*, **238**:1040–52. https://doi.org/10.1093/gji/ggae204
Peacock DCP, Sanderson DJ. 1991. Displacements, segment linkage and relay ramps in normal fault zones. *J Struct Geol*, **13**:721–33. https://doi.org/10.1016/0191-8141(91)90033-F
Scholz CH. 1998. Earthquakes and friction laws. *Nature*, **391**:37–42. https://doi.org/10.1038/34097
Segall P, Pollard DD. 1980. Mechanics of discontinuous faults. *J Geophys Res*, **85**:4337–50. https://doi.org/10.1029/JB085iB08p04337
Sethanant I, Nissen E, Pousse-Beltran L, Bergman E, Pierce I. 2023. The 2020 Mw 6.5 Monte Cristo Range, Nevada, earthquake: anatomy of a crossing-fault rupture through a region of highly distributed deformation. *Bull Seismol Soc Am*, **113**:948–75. https://doi.org/10.1785/0120220166
Sheng M, Chu R, Ni S, Wang Y, Jiang L, Yang H. 2020. Source parameters of three moderate size earthquakes in Weiyuan, China, and their relations to shale gas hydraulic fracturing. *J Geophys Res Solid Earth*, **12**:e2020JB019932. https://doi.org/10.1029/2020JB019932
Skoumal RJ, Ries R, Brudzinski MR, Barbour AJ, Currie BS. 2018. Earthquakes induced by hydraulic fracturing are pervasive in Oklahoma. *J Geophys Res Solid Earth*, **123**:10918–35. https://doi.org/10.1029/2018JB016790
Soliva R, Benedicto A. 2004. A linkage criterion for segmented normal faults. *J Struct Geol*, **26**:2251–67. https://doi.org/10.1016/j.jsg.2004.06.008
Soliva R, Benedicto A, Maerten L. 2006. Spacing and linkage of confined normal faults: importance of mechanical thickness. *J Geophys Res Solid Earth*, **111**:B01402. https://doi.org/10.1029/2004JB003507
Soliva R, Benedicto A, Schultz RA, Maerten L, Micarelli L. 2008. Displacement and interaction of normal fault segments branched at depth: implications for fault growth and potential earthquake rupture size. *J Struct Geol*, **30**:1288–99. https://doi.org/10.1016/j.jsg.2008.07.005
Stein RS, King GCP, Lin J. 1992. Change in failure stress on the southern San Andreas fault system caused by the 1992 magnitude = 7.4 Landers earthquake. *Science*, **258**:1328–32. https://doi.org/10.1126/science.258.5086.1328
Thomas AL. 1993. *POLY3D: A three-dimensional, polygonal element, displacement discontinuity boundary element computer program with applications to fractures, faults, and cavities in the Earth's crust*. Ph.D. Thesis, Department of Geology, Stanford University, 1993.
Wang B, Harrington RM, Liu Y, Kao H, Yu H. 2020. A study on the largest hydraulic-fracturing-induced earthquake in Canada: observations and static stress-drop estimation. *Bull Seismol Soc Am*, **110**:2283–94. https://doi.org/10.1785/0120190261
Wang M, Yang H, Fang L, Han L, Jia D, Jiang D, Yan B. 2020. Shallow faults reactivated by hydraulic fracturing: the 2019 Weiyuan earthquake sequences in Sichuan, China. *Seismol Res Lett*, **91**:3171–81. https://doi.org/10.1785/0220200174
Willemse EJM, Pollard DD, Aydin A. 1996. Three-dimensional analyses of slip distributions on normal fault arrays with consequences for fault scaling. *J Struct Geol*, **18**:295–309. https://doi.org/10.1016/S0191-8141(96)80051-4
Xi Y, Li J, Liu G, Cha C, Fu Y. 2018. Numerical investigation for different casing deformation reasons in Weiyuan-Changning shale gas field during multistage hydraulic fracturing. *J Pet Sci Eng*, **163**:691–702. https://doi.org/10.1016/j.petrol.2017.11.020
Yang H, Yao S. 2021. Shallow destructive earthquakes. *Earthq Sci*, **34**:15–23. https://doi.org/10.29382/eqs-2020-0072
Yi G, Long F, Liang M, Zhao M, Wang S. 2020. Geometry and tectonic deformation of seismogenic structures in the Rongxian-Weiyuan-Zizhong region, Sichuan Basin: insights from focal mechanism solutions. *Chin J Geophys*, **63**:3275–91. https://doi.org/10.6038/cjg2020O0095
Zaccagnino D, Doglioni C. 2023. Fault dip vs shear stress gradient. *Geosystems Geoenvironment*, **2**:100211. https://doi.org/10.1016/j.geogeo.2023.100211
Zhang F, Wang R, Chen Y, Chen Y. 2022. Spatiotemporal variations in earthquake triggering mechanisms during multistage hydraulic fracturing in Western Canada. *J Geophys Res Solid Earth*, **127**:e2022JB024744.
Zhang P. 2013. A review on active tectonics and deep crustal processes of the Western Sichuan region, eastern margin of the Tibetan Plateau. *Tectonophysics*, **584**:7–22. https://doi.org/10.1016/j.tecto.2012.02.021
Zhu L, Helmberger DV. 1996. Advancement in source estimation techniques using broadband regional seismograms. *Bull Seismol Soc Am*, **86**:1634–41. https://doi.org/10.1785/BSSA0860051634
Zi J, Yang Y, Yang H, Su J. 2025. The 11-month precursory fault activation of the 2019 ML 5.6 earthquake in the Weiyuan shale gas field, China. *Commun Earth Environ*, **6**: 175. https://doi.org/10.1038/s43247-025-02151-1

Received: September 29, 2024; Revised: February 13, 2025; Accepted: March 10, 2025